Materials Characterization 195 (2023) 112477

Contents lists available at ScienceDirect

Materials Characterization

journal homepage: www.elsevier.com/locate/matchar

Mapping 3D grain and precipitate structure during in situ mechanical testing of open-cell metal foam using micro-computed tomography and high-energy X-ray diffraction microscopy

Quinton C. Johnson [a], Peter Kenesei [d], Steve Petruzza [b,c], Jayden Plumb [a], Hemant Sharma [d], Jun-Sang Park [d], Elliott Marsden [a], Kristoffer Matheson [a], Michael W. Czabaj [a], Ashley D. Spear [a,*]

[a] Department of Mechanical Engineering, University of Utah, Salt Lake City, UT 84112, USA
[b] Scientific Computing and Imaging Institute, University of Utah, Salt Lake City, UT 84112, USA
[c] Department of Computer Science, Utah State University, Logan, UT 84322, USA
[d] Advanced Photon Source, Argonne National Laboratory, Lemont, IL 60439, USA

ARTICLE INFO

Keywords:
Microstructure
Synchrotron radiation
X-ray CT
Crystallography
Cellular metal
Lattice structure

ABSTRACT

Open-cell metal foams are ultra-low-density cellular metals with complex hierarchical structures that span bulk, cell, ligament, and sub-ligament scales and give rise to desirable properties such as high strength-to-weight ratio and excellent energy absorption. Although literature suggests that intrinsic material structures at sub-ligament length scales (e.g., grains and precipitates) play an important role in mechanical behavior of open-cell metal foams, there are very few experimental measurements of such structures in three dimensions and for meaningful volumes of foam. This study seeks to map and track the three-dimensional (3D) grain and precipitate structures of an intact volume of open-cell aluminum foam by advancing microstructural characterization techniques that leverage X-ray micro-computed tomography (μCT) and far-field high-energy X-ray diffraction microscopy (FF-HEDM). A 6%-relative-density aluminum foam sample was mechanically tested in compression while μCT and FF-HEDM measurements were collected at interrupted loading states at beamline 1-ID of the Advanced Photon Source. A new scanning strategy and reconstruction algorithm were established to enable characterization of a foam volume with diameter approximately four times wider than the nominal width of the X-ray beam. The result is a set of maps that detail both the 3D grain and precipitate structures throughout the foam volume at successive strain steps. A novel grain tracking procedure was developed to track individual grains within the foam volume by accounting for the large rigid-body motions that individual ligaments can undergo during mechanical loading. The ability to track grains and precipitate structures in three dimensions throughout large bulk deformation of ultra-low-density polycrystalline materials enables new possibilities for validating numerical models and investigating local failure mechanisms. Furthermore, the methods and procedures developed in this study could be applied to other ultra-low-density structures, such as additively manufactured lattices.

1. Introduction

Open-cell metal foams are ultra-low-density materials with a complex hierarchical structure that spans bulk, cell, ligament (or strut), and sub-ligament scales. This hierarchical structure lends itself to properties that make open-cell metal foams desirable candidates for multifunctional applications in which impact absorption, sound damping, heat transfer, and ultra-light-weight structural reinforcement are important [1]. There is an abundance of literature relating bulk- or cell-level characteristics of open-cell metal foams to mechanical or other properties (e.g., see Refs. [2–6]). Perhaps the most well-known of which is the Gibson-Ashby model [7–9], which relates the plastic collapse strength of open-cell foam to its relative density.

In recent years, there has been work reported in the literature suggesting that intrinsic material structures at sub-ligament scales influence the mechanical properties of open-cell metal foams. For example, Zhou et al. [10] investigated the effects of various heat treatments on mechanical response of aluminum 6101 open-cell foams and found that T6 heat-treated foams had higher yield strengths and greater ability to strain harden compared to foams in the as-cast or annealed condition;

* Corresponding author.
E-mail address: ashley.spear@utah.edu (A.D. Spear).

https://doi.org/10.1016/j.matchar.2022.112477
Received 19 September 2022; Received in revised form 9 November 2022; Accepted 10 November 2022
Available online 16 November 2022

this effect was attributed to the presence of homogeneously distributed fine silicon precipitates that served to hinder dislocation motion. In fact, second-phase precipitates have been reported in many studies to significantly impact the failure mechanisms of individual ligaments in open-cell metal foams [3,10–14]. Generally, these brittle precipitates exhibit low fracture toughness and poor strain compatibility with the surrounding matrix, acting as preferred crack nucleation sites that eventually lead to brittle ligament fracture. Grain structure has also been found to influence mechanical behavior of open-cell metal foams. For example, Zhou et al. [15] performed microtensile tests on individual ligaments excised from open-cell aluminum foam and found that, not only does mechanical response depend upon heat treatment, but that the response of the individual ligaments deviates from that of the bulk material, suggesting that grain-structure-dependent size effects play a role in the mechanical behavior of open-cell metal foams. In other work, Goussery et al. [16] used electron backscatter diffraction (EBSD) to analyze the grain structure in hollow-strut, open-cell, nickel foams and found that compressive yield strength of the foams exhibited a Hall–Petch-like response that eventually saturated once the grain sizes spanned the wall thickness of the hollow struts. Recent work by Wang et al. [17] demonstrated for the first time the capability of adaptively refining the grain size within open-cell Mg foams while keeping the strut-scale geometry constant using a multi-axial forging process. Similar to the work by Goussery et al. [16], Wang et al. [17] showed that yield strength and plastic collapse strength of the Mg foams varies as a function of grain size.

While the aforementioned studies highlight the importance of considering sub-ligament structures in investigating the mechanical response of open-cell metal foams, the experimental observations (viz., of grain structure) reported thus far in the literature have been limited to two-dimensional (2D) characterization methods, which generally involve polishing or etching sections of a sparsely populated foam volume and using optical or electron imaging techniques. There is one exception, which is recent work done by Plumb et al. [18], in which a high-energy X-ray diffraction microscopy (HEDM) technique was used to characterize three-dimensional (3D) grain structure in individual ligaments of an open-cell aluminum foam. However, due to experimental limitations (which are addressed in this work), the foam volume had to be deconstructed into individual ligaments, consequently precluding any subsequent mechanical testing of an intact foam volume. Thus, there remains a need to measure and track the 3D grain structure for intact volumes of open-cell metal foams, thereby enabling new insights relating sub-ligament material structures to mechanical response.

HEDM techniques available at third-generation synchrotron light sources [19] provide an opportunity to characterize nondestructively the 3D grain and sub-grain structures in polycrystalline materials. Such techniques have been applied to a range of metal alloys, including magnesium [20,21], titanium [22], nickel [23], and aluminum [24]. Two modalities of HEDM are commonly used: near-field (NF) and far-field (FF). The reader is referred to Refs. [25–30] for detailed descriptions of each modality. Pokharel et al. [31] presented one of the first studies to apply HEDM (in a NF modality) concurrently with in situ mechanical loading to observe and analyze statistically significant bulk 3D grain evolution for full local neighborhoods of individual grains in a polycrystalline material. Since then, others have reported the concurrent use of HEDM with in situ mechanical testing to characterize and track the evolution of grain structure and grain-structure-dependent micromechanical response in 3D [20,22,32–34]. Detailed reviews of such experiments are provided in Refs. [29,35,36]. In such studies, a polycrystalline sample is deformed to moderate levels (less than few percent macroscopic strain). Grain position and crystal misorientation thresholds are typically sufficient to track individual grains and their micromechanical state within the polycrystal and understand how the grains accommodate local stress concentration and incompatibilities.

The task of tracking grains in 3D throughout applied mechanical loading of ultra-low-density, open-cell structures presents two unique challenges compared to doing so in a fully or mostly dense material. First, individual ligaments can undergo large motions during loading; this rigid-body motion of ligament and local crystal lattice rotation need to be deconvolved appropriately to confidently track individual grains between applied-strain steps. Second, open-cell structures need to be much larger to obtain a representative volume element compared to a fully dense counterpart, making open-cell structures unsuitable for a typical HEDM data-acquisition and analysis strategy.

The goal of this work is to address the above-described challenges by establishing a framework to map and automatically track 3D grain structure by combining FF-HEDM and absorption contrast micro-computed tomography (μCT) for a complete, intact volume of open-cell aluminum foam subject to in situ compressive loading. This is accomplished by implementing a new HEDM data acquisition and analysis method in concert with a ligament-tracking procedure that enables expressing crystal orientations relative to time-dependent ligament reference frames. The resulting reconstructions allow the ligament, grain, and precipitate structures for an open-cell metal foam to be visualized in three dimensions and subsequently tracked through large deformation.

2. Experimental methods, reconstruction, and data integration

2.1. Material and high-energy X-ray experiments

A sample of 40 pore-per-inch (PPI), 6% dense, aluminum 6101-T6 foam manufactured via investment casting [37] was selected for the compression experiment. A cylindrical volume with diameter and height of approximately 5 mm was machined from a bulk sample of foam using wire electrical discharge machining.

The experiments were conducted at beamline 1-ID of the Advanced Photon Source (APS). A custom, portable load frame developed by Matheson et al. [38] that allows uninterrupted illumination of the sample throughout 360° rotation was used to compress the foam sample. The load frame was installed on a stage stack described in [39] with sufficient degrees-of-freedom to move and align the sample and the rotation axis with respect to the incident high-energy X-ray beam. The energy of the incoming X-ray beam was 61.33 keV. The sample was compressed in displacement control to four displacement levels: 0.0 mm (unloaded state), 0.74 mm, 1.71 mm, and 2.70 mm (54% final applied strain). At each displacement step, the loading was paused, and X-ray μCT and FF-HEDM data were acquired. Following data reconstruction (detailed in Section 2.2), the μCT scans provided the overall foam and precipitate structure based on absorption contrast, and the FF-HEDM scans provided the grain center-of-mass (COM) positions and attributes associated with each COM, including crystallographic orientation, grain equivalent radius, confidence index, and elastic strain tensor.[1]

For μCT, an imaging detector developed and built at the APS was placed at 100 mm distance from the sample to optimize phase contrast. The beam size was 2.05 mm (horizontal) by 1.1 mm (vertical). Because the sample diameter was larger than the horizontal beam size, a stitching tomography approach was used, in which the rotation axis was translated in x_{Lab} (see Fig. 1 for reference coordinate system) to −1.95 mm, 0.0 mm, and 1.95 mm while keeping the sample aligned to the rotation axis to acquire enough radiographs for tomographic reconstruction of a 1.1 mm-tall sample layer. At each rotation axis position, the sample was rotated 360° and radiographs were acquired at every 0.1° increment. Further details of this stitching tomography strategy can be found in Ref. [40]. In the undeformed state, six layers were mapped covering the entire height of the foam sample, with overlap between the layer scans to facilitate merging the layers. In the subsequent applied-

[1] Tracking individual grains in deforming open-cell foam is a necessary step toward tracking grain-averaged strain evolution. However, strain analysis in the foam is beyond the scope of the current study and is not reported here.

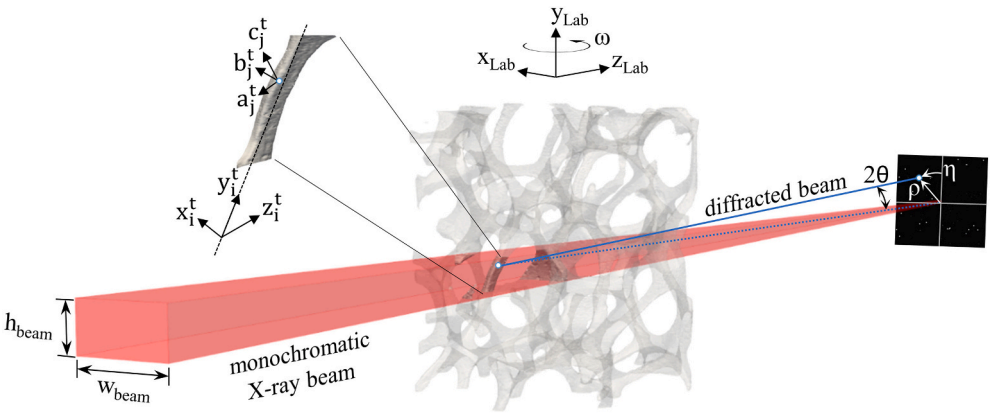

Fig. 1. Schematic of the far-field HEDM setup at the APS and the three relevant coordinate systems at a given time, *t*, during in situ mechanical loading of open-cell foam: laboratory reference frame (x_{Lab}, y_{Lab}, z_{Lab}), local reference frame for i^{th} ligament (x_i^t, y_i^t, z_i^t), and crystal reference frame for j^{th} grain (a_j^t, b_j^t, c_j^t). All coordinate systems are right-handed. The laboratory reference frame remains fixed over time. In this experiment, h_{beam} is 0.6 mm, w_{beam} is 1.2 mm, and the diameter of the foam sample is 5 mm.

displacement steps, as the sample height was reduced, the number of tomography layers was proportionally reduced. An animation demonstrating the scanning technique is provided in the online version of this article.

FF-HEDM measurements were performed using a box beam with a height of 0.6 mm and a width of 1.2 mm, as illustrated in Fig. 1. For FF-HEDM, a GE 41RT amorphous silicon area detector with 0.2 mm pixel size [41] was placed 813 mm downstream of the sample to capture enough diffraction rings for FF-HEDM reconstruction. The instrument geometry as illustrated in Ref. [39] was calibrated using CeO_2 and Au cube particle as described in [42–44]. Because the foam sample had a diameter of 5 mm, which was at least four times wider than the beam width, a new FF-HEDM scanning technique was established that allowed characterization of the entire sample. Similar to the stitching tomography strategy, the rotation axis was translated in x_{Lab} by multiples of incident beam width (1.2 mm). For each 0.6 mm-tall layer, a total of five x_{Lab} translations were necessary (−2.4 mm, −1.2 mm, 0.0 mm, +1.2 mm, and +2.4 mm). At each rotation axis position, the sample was rotated a full 360° in increments of 0.25°, and a diffraction pattern was acquired at each ω increment. The area detector acquired diffraction spots from the illuminated crystallographic planes satisfying the diffraction (Bragg) condition [28]. This new scanning strategy allowed to merge the diffraction patterns acquired at the same ω position and ultimately generate a grain map of a layer that is substantially larger than the incident horizontal beam size. A sufficient number of layers was scanned to cover the entire sample height, which was reduced with each displacement step due to compression.

2.2. Data reconstruction

2.2.1. Tomography reconstruction

Raw μCT data were reconstructed at the APS using an in-house software, TomoProc, which properly unified (stitched) the separately collected data with overlapping fields of view, corrected for the rotation axis alignment, and, after using Gridrec reconstruction algorithm [45], provided a stack of high-resolution (pixel size of 1.172 μm) grayscale images for each displacement step. The image stacks from multiple layers were registered using the overlapped regions and merged to create a single image stack for each displacement step. To reduce memory requirements, the image resolution was downsampled from 1.172 μm to 3.516 μm. The 3D image processing software Avizo (FEI Visualization Sciences Group) was then used to threshold the image stacks and manually segment the foam volume from the surrounding air. The segmented foam volume was exported as an stl file. To prepare the μCT data for integration with the FF-HEDM data set, the stl file for each displacement step was converted to a voxelized representation of the binarized foam with a downsampled resolution of approximately 25 μm.

Second-phase precipitates were segmented using a separate workflow based on multi-class segmentation (foam, precipitate, background) of the 16-bit full resolution (1.172 μm voxel size) grayscale tiff images. First, thresholding was performed for pixels with intensity values below the brightest 4.85% of pixels, and binary image stacks were saved as 8-bit images with solid foam regions labeled with an intensity of 255 and background with 0. Second-phase precipitates were segmented separately using the full resolution (1.172 μm voxel size) grayscale tiff images masked by the solid foam binary images. Precipitate structure segmentation was conducted using a U-net model [46] trained on a randomly sampled set of 10 hand-labeled images (out of approximately 12,600 images from all displacement steps). To create the final multi-class segmentation stack, voxels predicted to be precipitates were labeled in the 8-bit solid foam binary stack with intensity values of 100. For each displacement step, ImageJ [47] and Simpleware ScanIP software (Version S-2021.06; Synopsys, Inc., Mountain View, USA) were used to isolate the ligaments of interest from the 8-bit multi-class segmented stacks.

2.2.2. FF-HEDM reconstruction

Reconstruction of the foam grain structure from the stitching FF-HEDM was performed using Microstructural Imaging using Diffraction Analysis Software (MIDAS) [48,49], an in-house software developed at the APS. As indicated in Section 2.1, the diffraction patterns acquired with intentional translation of the rotation axis were merged prior to reconstructing the FF-HEDM data into the 3D grain map of a sample layer. For each layer, this procedure involved overlaying the translated diffraction datasets by coinciding the rotation axis for each dataset. Because each translation step of the rotation axis was selected as an integer multiple of the detector pixel size, the pixel boundaries were directly matched up, and the detected intensities on them were simply combined; no interpolation was necessary. For a given measurement layer, the algorithm generates a single dataset as the sum of translated datasets, which is then reconstructed using MIDAS.[2] The output consists of grain COM positions and attributes associated with each COM, including crystallographic orientation and grain equivalent radius. Finally, data from all measurement layers of a given displacement step were merged to generate a map of grain COM positions and associated attributes for the entire foam volume.

2.2.3. Data integration

Fig. 2 shows the grain COM positions from FF-HEDM superimposed on the μCT map of the foam sample measured in the unloaded state. The

[2] It was found that the ratio of diffraction spots assigned to grains versus the total number of diffraction spots (including orphaned spots) was approximately 90% at the sample reference state, but this number is anticipated to decrease with increasing applied load given the large deformation in portions of the foam during compression.

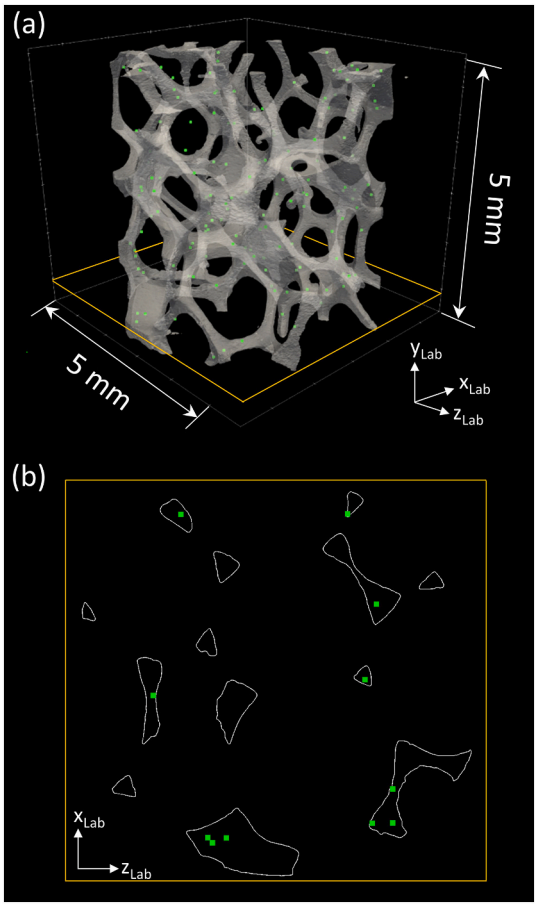

Fig. 2. After reconstruction and integration of the FF-HEDM and μCT data sets, the majority of the grain centroids fall within the volume occupied by the aluminum foam. (a) Three-dimensional view with a translucent foam volume and grain centroid positions plotted in green. (b) Cross-section view corresponding to the plane indicated in (a). Grain centroid data, plotted in green, from a single vertical FF-HEDM scan layer (approximately 0.6 mm in height) are superimposed over a 2D cross section view of the foam perpendicular to the loading direction.

majority of the gain COM positions fall within the boundaries of the foam ligaments, instilling confidence in the data acquisition procedure, reconstruction algorithm, and multi-modal data integration workflow developed specifically for the ultra-low-density foam sample.

While the FF-HEDM technique provides a map of grain COM positions and associated attributes, it does not provide a volume-filling map with complete grain morphologies. Therefore, a grain packing workflow was implemented using DREAM.3D [50] to approximate the 3D grain morphologies in the foam. Here, a summary of the workflow is presented; a more detailed presentation of the workflow is available in Tucker and Spear [51]. In the workflow, the grain-COM map from FF-HEDM and the map of foam volume from μCT, acquired at a particular displacement step, were first read into DREAM.3D. From the grain COM positions, the grains were grown using DREAM.3D's packing algorithms [50] until a cuboidal volume encompassing the extents of the foam volume was fully populated with grain structure. Once grain packing was complete, the binary foam mask was applied such that only voxels falling within the solid phase of the mask were retained; while voxels falling outside of the solid phase were converted to void space. After completion, the data were visualized in ParaView [52]. This process was performed for the foam volume measured at each displacement step.

2.3. Integration of ligament-tracking software

To automatically track individual ligaments within a sample of open-cell foam through large deformation, ligament tracking software developed by the Scientific Computing and Imaging Institute (SCII) at the University of Utah [53] was used in this work. Grayscale tomography image stacks corresponding to the four displacement steps (without precipitate structure resolved) were read into the software, and each ligament was identified using topology-based segmentation methods and tracked between steps based on spatial proximity. For each displacement step, the software computes and outputs the nominal radius, length, and orientation of each ligament. The orientation of the ligament longitudinal axis (y_i^t in Fig. 1) is provided in terms of direction cosine angles ($\theta_x, \theta_y, \theta_z$) expressed relative to the global reference frame. The tracking algorithm and software capabilities are described in detail by Petruzza et al. [53].

An overview of the process of tracking grains is illustrated in the flowchart in Fig. 3. Using length and radius data for the ligaments obtained from the SCII ligament-tracking software, an idealized cylindrical ligament volume was defined. Grains belonging to the idealized cylindrical volume of a particular ligament were assigned to that ligament and were labeled with a ligament ID number. For a given displacement step, *t*, the Bunge Euler angles for grain *j* were used to form a rotation matrix, $\mathbf{G_j^t}$, mapping from the global reference frame to the crystal reference frame (see Fig. 4). Then, using the ligament orientation data output from the SCII software, the task was to express the crystal orientation of the j^{th} grain relative to the local reference frame of the parent ligament to which the grain belongs (x_i^t, y_i^t, z_i^t), rather than relative to the global APS laboratory frame ($x_{Lab}, y_{Lab}, z_{Lab}$). Within the automated framework, this task was accomplished by first finding a rotation matrix, $\mathbf{R_i^t}$, for each ligament that would map the global reference frame (x_{Lab}, y_{Lab}, z_{Lab}) into the reference frame of the individual ligament given the direction cosine angle, θ_y, and assuming that the axis of rotation, $\hat{r}$, is normal to the plane containing y_{Lab} and y_i^t, as shown in Fig. 4. The latter assumption was necessary for the automated tracking procedure, as the SCII ligament-tracking software provides a vector describing the longitudinal axis of each ligament (y_i^t) but cannot currently track axes corresponding to x_i^t and z_i^t, which are not uniquely defined. Implicit in the above assumption is that the ligaments do not rotate (spin) about y_i^t throughout applied displacement. The rotation matrix $\mathbf{R_i^t}$ is found using the axis-angle form of the Euler-Rodriguez formula (see Brannon [54]):

$$\mathbf{R} = (\cos\alpha)[\mathbf{I} - \hat{r}\hat{r}] + \hat{r}\hat{r} + (\sin\alpha)[\hat{r} \times \mathbf{I}], \tag{1}$$

where α is the angle of rotation (θ_y in this case), $\mathbf{I}$ is the identity tensor, $\hat{r}\hat{r}$ is a vector-vector dyad, and $[\hat{r} \times \mathbf{I}]$ is the skew-symmetric axial tensor associated with the rotation axis $\hat{r}$, which can be written as:

$$[\hat{r} \times \mathbf{I}] = \begin{bmatrix} 0 & -r_3 & r_2 \\ r_3 & 0 & -r_1 \\ -r_2 & r_1 & 0 \end{bmatrix}. \tag{2}$$

The implementation was verified by applying the rotation matrices $\mathbf{R_i^t}$ corresponding to an arbitrary subset of ligaments to the vector $\hat{y}_{Lab} = [010]$ and overlaying the transformed vectors onto the tomographic reconstructions of the ligaments to visually ensure proper alignment. Subsequently, the rotation matrix $\mathbf{R_i^t}$ was used to map the original orientation matrix, $\mathbf{G_j^t}$, to a new orientation matrix $\mathbf{Q_{ij}^t}$, which represents the crystal orientation of grain *j* expressed with respect to the reference frame of ligament *i* at displacement step *t*.

Once grains were assigned to ligaments and their crystal orientations were represented with respect to the local ligament reference frame, the task of tracking grains from one displacement step to the next became tractable. Namely, $\mathbf{Q_{ij}^t}$ for all detected grains belonging to a given ligament in one displacement step were compared to $\mathbf{Q_{ij}^{t+1}}$ for all detected

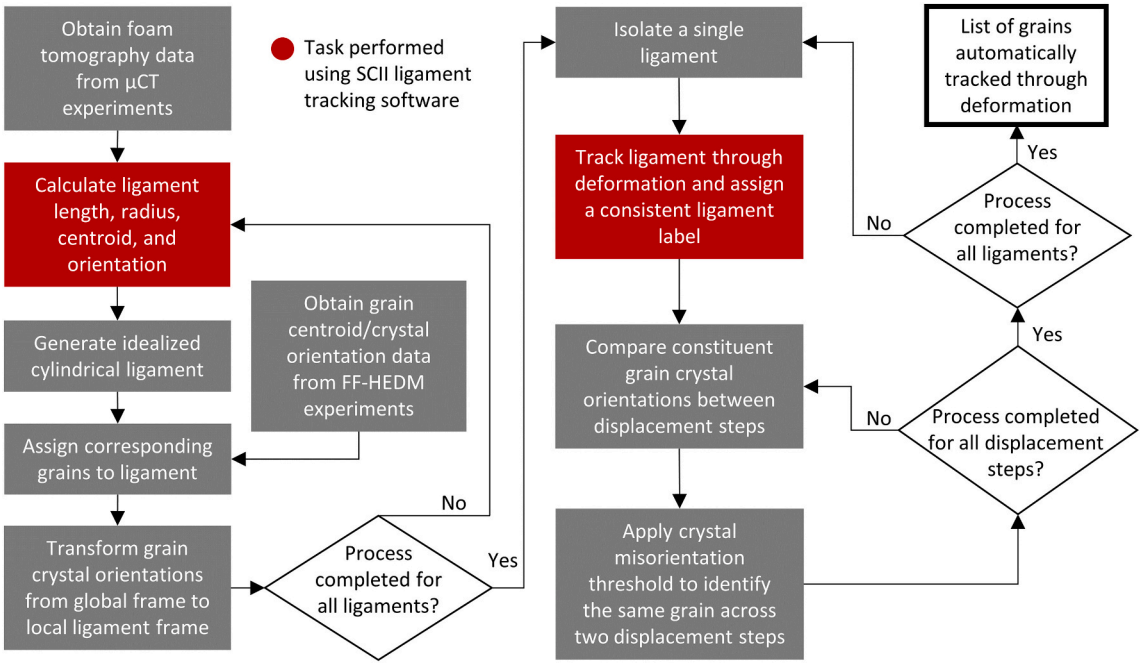

Fig. 3. High-level overview of the steps required to track grains through large deformation. A combination of ligament- and grain-orientation data are required to enable grains to be identified and tracked through deformation in an open-cell foam. Red boxes correspond to tasks performed using the ligament-tracking software; gray boxes correspond to tasks performed using a combination of in-house codes and custom-built scripts.

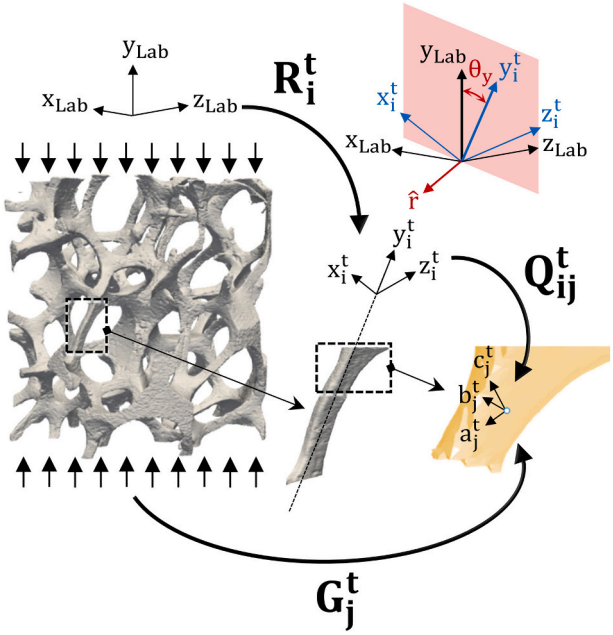

Fig. 4. Visualization of coordinate transformations used to express the crystal orientation of grain *j* relative to the reference frame of ligament *i* to which the grain belongs. Superscript *t* denotes the applied-displacement step. The global (laboratory) reference frame remains fixed throughout the experiment. All coordinate systems are right-handed.

grains belonging to that same ligament in the subsequent displacement step. Then, a crystallographic misorientation criterion was applied (in the local ligament reference frame) to the subset of detected grains belonging to the given ligament. A misorientation threshold of 10° was applied to track grains between displacement steps.

3. Results

3.1. Mechanical behavior

Fig. 5 shows the force versus displacement data gathered during the in situ compression experiment. The precise points at which loading was halted and scanning occurred for each displacement step are indicated. Initially, the force does not increase with displacement, as the foam is not fully in contact with the compression platens. Then, the force initially increases linearly with displacement until the ligaments yield and undergo complex deformation. Insets in Fig. 5 show 3D reconstructions of the μCT data for each displacement step, illustrating the large deformation of the ligaments.

3.2. 3D grain maps

Fig. 6 shows the results of μCT and FF-HEDM data integration using the framework described in Section 2.2.3. Fig. 6a shows the foam volume in the undeformed state. The volume at each subsequent displacement step is depicted in Fig. 6b–d, successively. Crystal orientation is represented by an inverse pole figure (IPF) color map with the loading axis as the reference direction. Note that the IPF color maps do not generally show a one-to-one correspondence between displacement steps, as the crystal orientations represented in Fig. 6 are expressed with respect to the global (laboratory) reference frame. In total, 141 grains were detected in the undeformed foam volume. Subsequently, 153, 166, and 155 grains were detected in the first, second, and third displacement steps, respectively. Reasons for the discrepancy between number of detected grain are discussed in Section 4.3.

Results from the ligament and grain tracking procedure described in Section 2 are illustrated in Fig. 7, in which grains that were automatically tracked from the undeformed state to the first displacement step are colored by grain ID, and grains shown in gray were unable to be tracked between the two displacement steps. Of the 141 grains detected in the initial, undeformed foam volume, the framework was successful in automatically tracking 83 (59%). Subsequently, 70 of 153 grains (46%) were tracked from the first to second displacements step, and 45 of 166

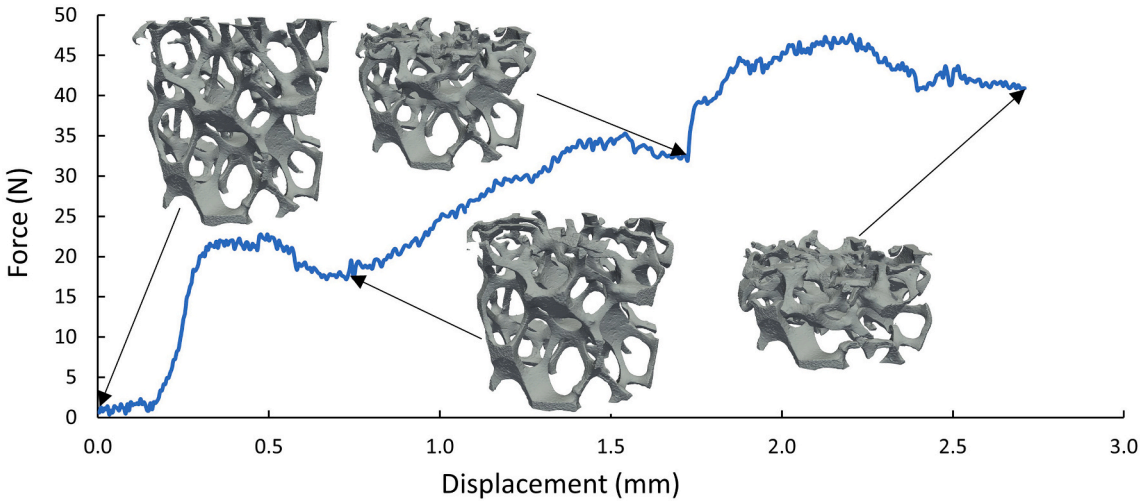

Fig. 5. Force versus displacement response for an in situ compression experiment of an open-cell aluminum foam performed at the APS 1-ID beamline. Displacement was held fixed at the following steps to allow μCT and FF-HEDM scanning: 0.00, 0.74, 1.71, and 2.70 mm. Insets show the 3D reconstructed representation of the foam volume at each displacement step.

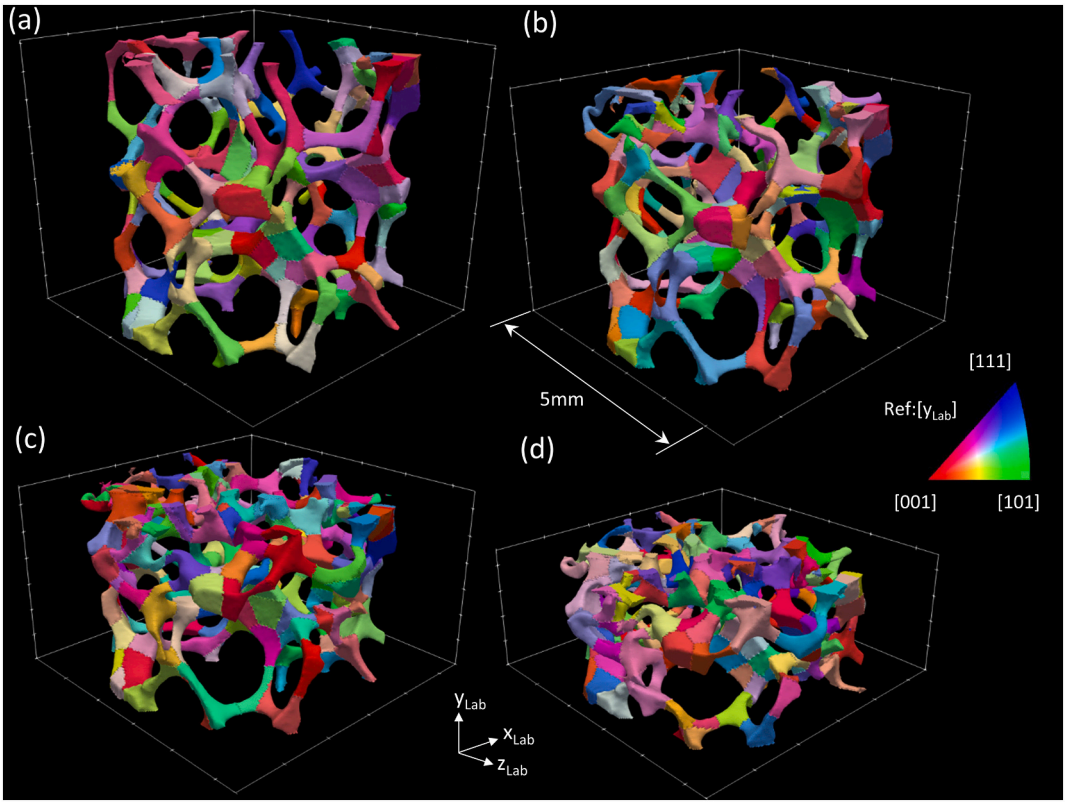

Fig. 6. Three-dimensional grain maps at each of the four applied displacement steps: a) 0.00 mm, b) 0.74 mm, c) 1.71 mm, and d) 2.70 mm. The crystal orientation of each grain is represented using standard IPF colors with the y_{Lab}, or loading axis, as the reference direction.

grains (27%) were tracked from the second to third displacement step. Interestingly, the total number of unique grains that were automatically tracked and retained throughout all four displacement steps was 25, indicating that not all of the grains tracked to the second and third displacement steps were identified in the undeformed state of the foam. Fig. 8 shows the 25 unique grains that were tracked throughout the entire experiment. Reasons for this phenomenon are discussed in Section 4.3.

3.3. Precipitate structures

Fig. 9 shows the precipitate structures based on the segmented high-resolution μCT data. In the figure, nine ligaments are called out to provide magnified views of the precipitate content. The nine ligaments collectively represent three modes of ligament failure observed in the aluminum foam: brittle fracture, ductile fracture, and plastic collapse (i.e., significant plastic deformation with no fracture observed by the end of the experiment). The precipitate concentrations (by volume percentage), as determined from μCT, are reported for each ligament. The

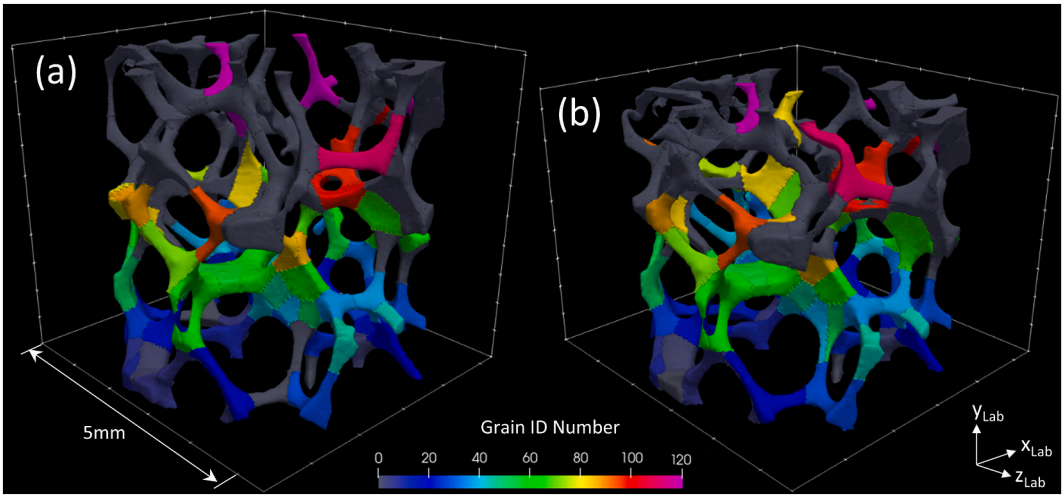

Fig. 7. Three-dimensional grain maps showing the ability of the framework to automatically track grains between successive displacement steps: a) undeformed state b) first displacement step. The color map represents the grain IDs for each of the automatically tracked grains. Grains depicted in gray were unable to be tracked.

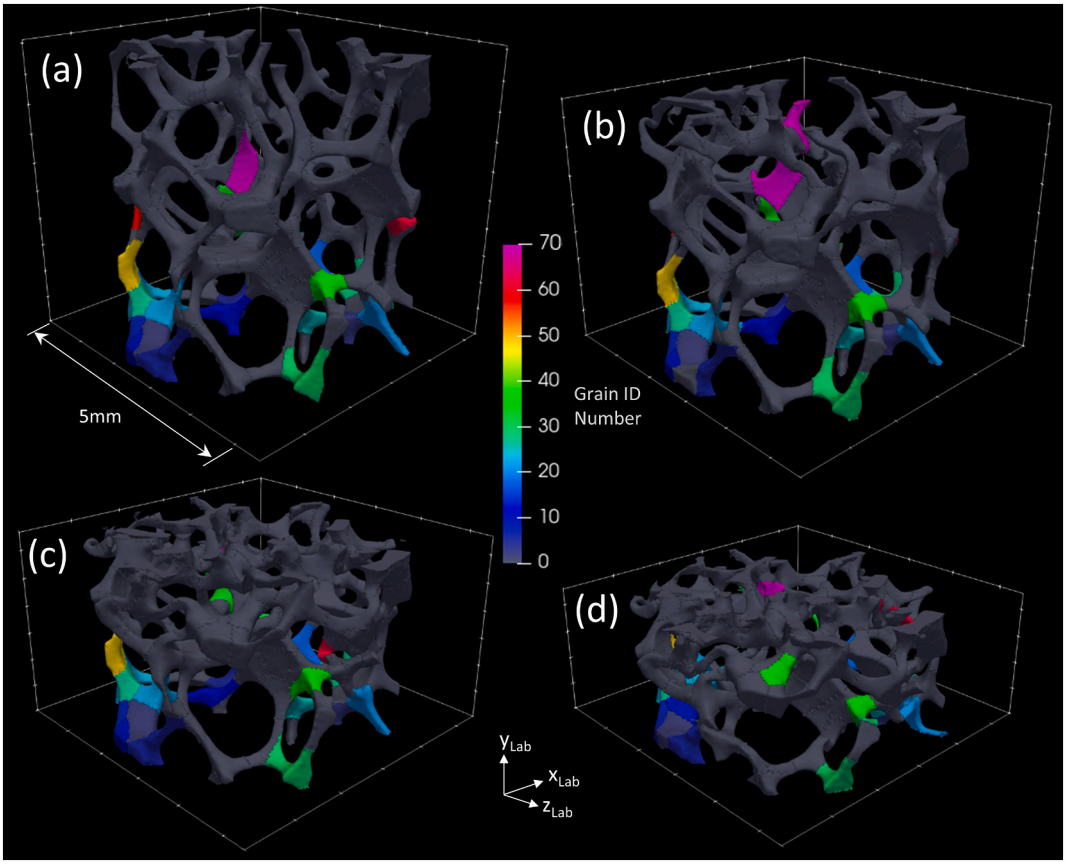

Fig. 8. Three-dimensional grain maps highlighting grains automatically tracked throughout all four displacement steps: a) 0.00 mm, b) 0.74 mm, c) 1.71 mm, and d) 2.70 mm. The color map represents unique grain IDs. Grains colored in gray were not able to be tracked automatically throughout the entire experiment.

quantitative analysis of precipitate content among the nine selected ligaments suggest that there is a correlation between the total precipitate concentration in a given ligament and the corresponding mode of failure. Specifically, ligaments with relatively high concentrations of precipitates tend to fail by brittle fracture, while those with relatively low concentrations tend to fail by ductile fracture or plastic collapse. Fig. 10 illustrates the evolution of ligament deformation and failure for each of the three failure modes. These observations provide valuable input to numerical models, which remains the topic of ongoing work by the authors. Further investigation is needed to fully explore local failure mechanisms in open-cell metallic foams and their dependence on precipitate structures, which is beyond the scope of the current work. Nonetheless, the results presented here demonstrate the utility of combining high-resolution μCT imaging with in situ mechanical testing to observe possible links between second-phase precipitate structures and failure mechanisms in open-cell foam.

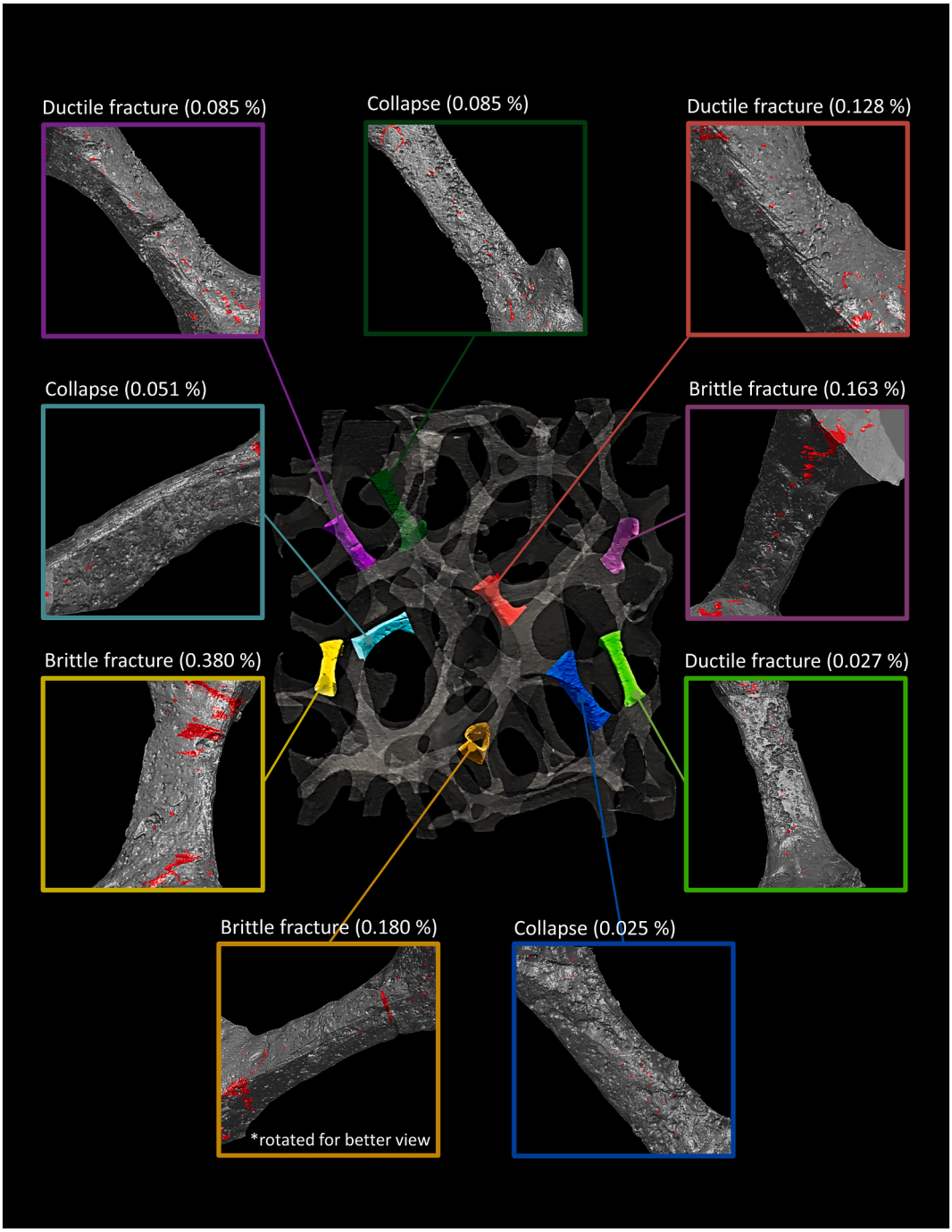

Fig. 9. Three-dimensional precipitate structures reconstructed from μCT data of a 5 mm-diameter sample of open-cell aluminum foam, shown in the undeformed state. Magnified views of precipitate content are called out for nine ligaments that collectively represent three observed modes of ligament failure: brittle fracture, ductile fracture, and (plastic) collapse. Precipitate structures are depicted in red, and precipitate concentrations by volume percentage are reported in parentheses.

4. Discussion

4.1. Grain structure observations

The framework developed for this study combines in situ 3D grain data from FF-HEDM and foam structure data from μCT to produce the 3D grain maps presented in Fig. 6. To the authors' knowledge, this is the first time that the 3D grain structure of a complete volume of an ultra-low-density metallic foam has been characterized by these two methods. Previously, individual ligaments were excised from a bulk sample of open-cell aluminum foam and were characterized individually using FF-HEDM by Plumb et al. [18]. The approach in the work by Plumb et al. [18] not only limited the total volume of foam that could be virtually reconstructed due to the time required for sample setup of each ligament, but also precluded the ability to perform any subsequent mechanical testing of the foam because the sample had to be partially deconstructed to collect the data. However, using the methods presented herein, a complete and intact volume of foam was characterized that was four times wider than the width of the FF-HEDM beam. This was made possible using the new data acquisition method and stitching algorithm for data reconstruction described in Section 2. The new framework not only enables in situ mechanical testing on bulk foam samples containing

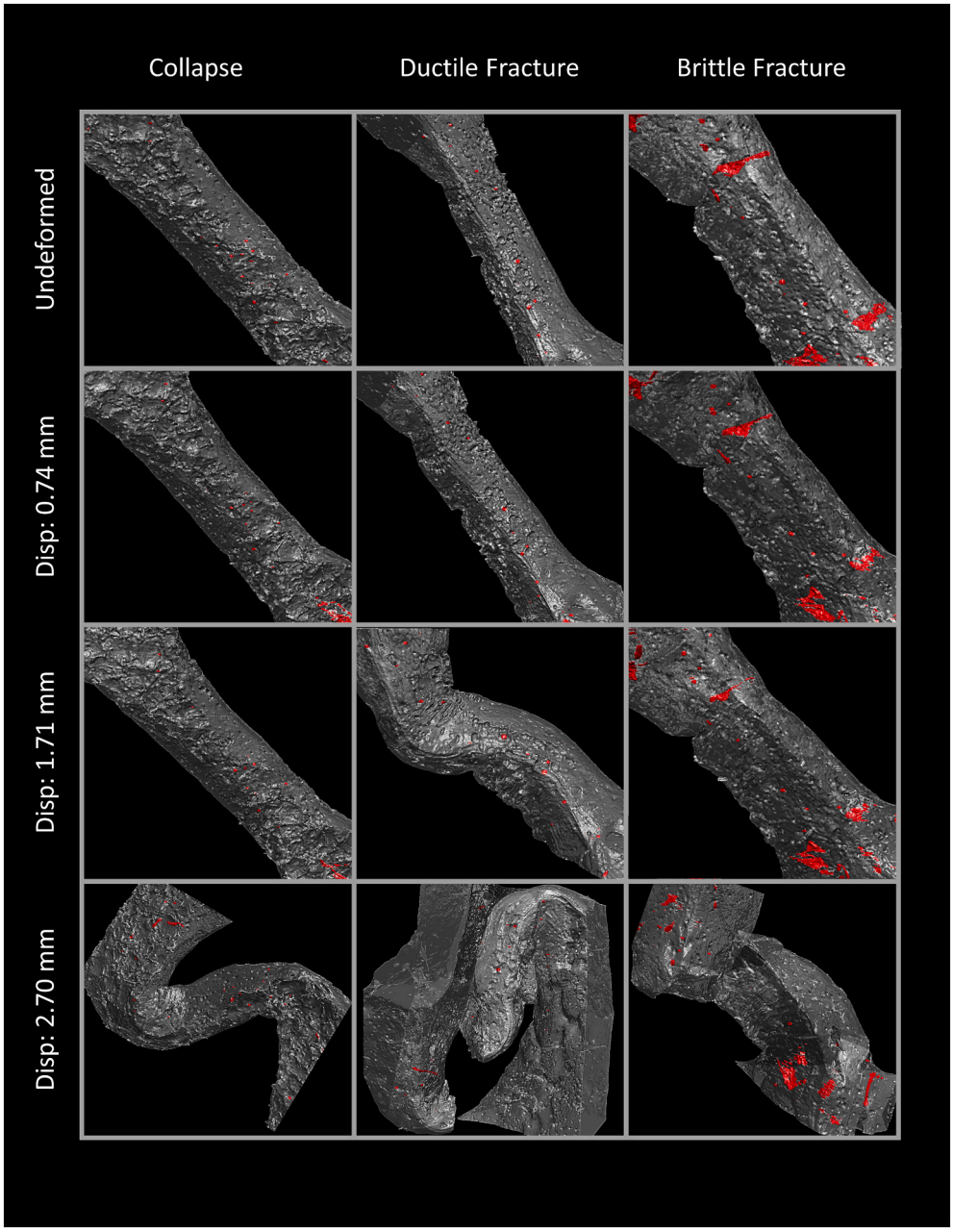

Fig. 10. Reconstructed μCT data at four incremental displacement steps for three ligaments representing three observed modes of ligament failure: (plastic) collapse, ductile fracture, and brittle fracture. Precipitate structures are depicted in red.

multiple complete unit cells, it also opens up a wide range of possibilities for interrogating similar ultra-low-density samples (e.g., additively manufactured lattice structures) that were previously deemed too large for this characterization method.

The unique 3D grain maps generated as a result of this experiment provide valuable insight into the size, distribution, and crystal orientation of grains in open-cell metallic foam. The proposed framework allows verification of grain-scale observations that were previously limited by 2D measurements. For example, we can confirm previous 2D observations [3,12,55] that grains are large relative to the size of individual ligaments in open-cell investment-cast foams, and verify that most ligaments are comprised of only one or two through-thickness grains. Before, observations of crystallographic orientation through EBSD analysis in open-cell foams were limited to 2D planar slices [38,55]. The framework presented herein provides a means of visualizing and quantifying, for the first time, the complete 3D grain structure for meaningful volumes of ultra-low-density polycrystalline materials.

4.2. *Comparing grain-boundary approximation with 3D precipitate maps*

An attempt was made to compare the accuracy of the grain boundaries produced via the packing algorithm in DREAM.3D to known grain boundary locations based on distributions of precipitate structures observed in the μCT reconstructions. Work by Zhou et al. [3] showed that for an investment-cast aluminum 6101 open-cell foam similar to the foam studied here, particle clusters with a chemical composition consisting of Al, Si, Fe, and Mg tend to form along grain boundaries in the foam ligaments. Similarly, Amsterdam et al. [12] showed that some grain boundaries in a similar sample of open-cell aluminum 6101 foam were decorated by second-phase AlFeSi precipitates. While not all grain boundaries observed by Amsterdam et al. [12] were populated with precipitates, backscatter electron images of grain boundaries indicated

that when non-isolated precipitate concentrations (i.e., clusters) were identified, they were located at grain boundaries. Based on these observations reported in the literature, we assume that semi-continuous, planar precipitate accumulations observed in the 3D μCT reconstructions, as seen in Fig. 11(a,c,e), indicate grain boundaries in the foam ligaments.

In our analysis, we noted two types of precipitate accumulations that assist in determining whether or not the precipitates lie on a grain boundary. The first type consists of precipitates clumped into small, isolated regions. These isolated precipitate structures were randomly distributed throughout the volume of the ligament, and with no a priori knowledge of the grain boundary location, we have no definitive way of determining whether or not these precipitates coincide with grain boundaries. However, the second type of precipitate accumulation is represented in Fig. 11(a,c,e) and consists of large clusters of precipitates distributed fairly continuously along a plane that bisects the width of a given ligament. Given their planar distribution and the results presented by others in the literature (discussed above), it is likely that such precipitate clusters coincide with grain boundaries.

By reasonably assuming that semi-continuous, planar precipitate accumulations observed in the 3D μCT reconstructions are coincident with grain boundaries, we visually gauged the accuracy of the grain-boundary approximation generated by DREAM.3D. As described in Section 2, grain morphology is approximated by DREAM.3D's grain-packing algorithms, in which grain centroid positions and relative size parameters are used as inputs. Fig. 11 shows three ligaments with planar precipitate concentrations (a,c,e), indicating grain boundary locations, alongside the approximated 3D grain structure (b,d,f). The first ligament shows very good qualitative agreement between known and approximated grain boundary locations. Three grain boundaries are present in each representation, two of which show very good alignment between the approximated grain boundary and the observed planar precipitate structures. The second ligament shown in Fig. 11(c,d) includes four grain boundaries for both the known and approximated cases, and their general locations agree. Furthermore, three of the grain boundaries show very similar alignment with the planar distribution of precipitates for that ligament. In the final case (Fig. 11(e,f)), four distinct grain boundaries are identified for both the known and approximated cases. However, in contrast to the first two cases, grain boundaries appear to intersect at different points in the precipitate maps when compared to the approximated case. Despite slight differences in grain boundary morphology in the final case, the analyzed data, taken as a whole, show reasonable qualitative agreement between known grain boundary locations and the approximated grain boundaries generated by DREAM.3D. While this validation is strictly qualitative, it provides insight into the accuracy of the approximated grain boundaries

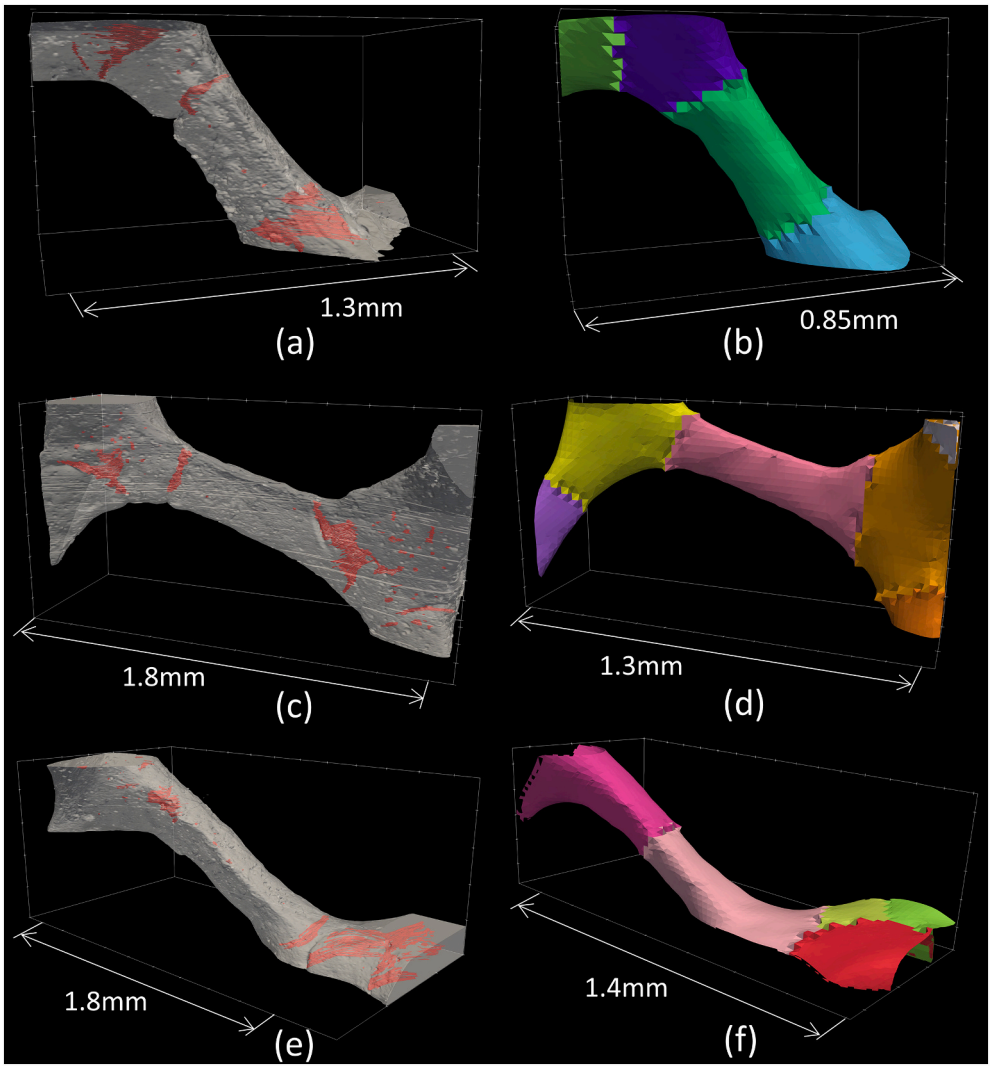

Fig. 11. Three-dimensional grain maps for three individual ligaments comparing the actual grain boundary locations (presumed based on planar concentrations of precipitate clusters) with grain boundary approximations generated by the DREAM.3D pipeline.

generated by DREAM.3D and subsequently the accuracy of the representation of the 3D grain maps produced using the methodology presented herein.

4.3. Grain tracking

A major contribution of this work is the ability to characterize and automatically track grains throughout large deformation of an ultra-low-density, open-cell structure. This task requires information about the orientation of individual ligaments, which we obtained from the SCII ligament-tracking software described in Section 2.3. Crystal orientation data were transformed into the local ligament reference frame, which then enabled grain tracking by applying a misorientation threshold between displacement steps.

As described in Section 3.2 and illustrated in Fig. 7, some of the grains identified in one step were not identified in subsequent steps, or vice versa. This is attributed to two main factors. First, the total number of grains identified from the FF-HEDM measurements does not remain constant throughout the experiment. Even for fully dense materials that do not undergo significant deformation during in situ mechanical testing with FF-HEDM imaging, others have reported in the literature slight inconsistencies in the total number of grains detected from scan to scan in a fixed volume of material. For example, Naragani et al. [23] attributed such observed inconsistencies to fluctuations in illuminating X-ray flux and to various software reconstruction limitations. In such case, the total number of detected grains does not systematically increase or decrease throughout the experiment, but instead shows small fluctuations between displacement steps. Second, we suspect that in the case of tracking grains throughout large deformation in open-cell aluminum foam, some grains might have undergone true crystallographic rotation upon large deformation, causing formerly low-angle grain boundaries to be classified as high-angle grain boundaries. A number of studies have demonstrated the propensity of grains in polycrystalline aluminum to undergo true rotation when subjected to tensile or shear loading [56–58]. Such crystallographic reorientation could lead to the detection of new grains that did not appear in previous displacement steps, which might explain why, of the 45 grains tracked from the second to third displacement step, only 25 were tracked throughout the entire experiment, beginning with the undeformed state.

Another possible explanation for why not more than 25 grains were tracked throughout the experiment is the inability to fully characterize the orientations of the ligaments using the current version of the SCII ligament-tracking software. Recall from Section 2.3 that the orientation provided from the SCII software is a vector describing the orientation of the longitudinal axis of the ligament with respect to the global coordinate system. However, the software does not track the orientation of the other two ligament basis vectors (i.e., we have no information regarding the rotation of a given ligament about its longitudinal axis). As such, when grain-orientation representations are transformed from the global reference frame to the local ligament reference frame, an assumption is made that the plane perpendicular to the longitudinal axis undergoes no rotation about the longitudinal axis. This approximation provides us with accurate enough data to be able to track the grains through deformation but does not allow us, as of yet, to track the crystal lattice rotation through deformation. We estimate the orientation of a grain, with respect to its local ligament reference frame, to be off from the actual value by anywhere from 0–15°. The authors recommend future research to focus on improving the orientation description of the local ligament coordinate system so that a more accurate crystal orientation description for grains with respect to the local ligament reference frame can be achieved.

Some of the challenges described above could potentially be resolved by taking smaller displacements steps between imaging, which leads to smaller orientation changes between steps. As illustrated in Fig. 7, for example, the majority of ligament deformation occurring within the first displacement step was localized in the top portion of the foam, while the ligaments in the middle and lower portions remained relatively undeformed. Correspondingly, the majority of automatically tracked grains between the undeformed and first displacement steps were located in the region of foam below the zone of significant localized deformation. Taking smaller displacement steps between imaging could increase the likelihood of tracking more grains throughout deformation. Some considerations in the design of experiment that affect the determination of target displacement increments include the sample size of the foam (hence, the number of subscans required to fully characterize the volume and corresponding time required to collect them), the desired value of final displacement to be applied (greater than 50% in this work), and the amount of allocated beamtime. These parameters can be optimized on a case-by-case basis, depending on the overarching aims of a given experiment.

4.4. Limitations and implications

There are four primary limitations of the current method implementation. First, the ability to track grains breaks down for grain centroids located in or very near nodal junctions of the foam. In such cases, the assignment of grains to unique ligaments—which is required to express the crystal orientation relative to the ligament reference frame—becomes ambiguous. Thus, the uncertainty in grain tracking is higher for those grains that primarily occupy nodal junctions than those primarily occupying ligaments. Second, if ligaments rotate significantly about their longitudinal axis (y_i^L) during applied displacement, then the likelihood of tracking grains within those ligaments diminishes as the error in representing crystal orientation relative to ligament reference frame increases (Section 2.3 describes the assumption regarding ligament rotation). Third, severe plastic deformation of the ligaments can lead to decreased confidence in the ability to index crystal orientations using FF-HEDM, which would subsequently decrease grain tracking ability in regions of foam undergoing significant plastic collapse. Finally, as discussed extensively in Section 4.2, the grain boundary characteristics are not measured directly using FF-HEDM; rather, they must be approximated using a grain-packing algorithm informed by the experimental diffraction data. Although the approximation is shown to be reasonably accurate, there could be applications for which more accurate representation of grain boundaries is required. An alternative technique is NF-HEDM [24–26,59], which allows to reconstruct 3D grain geometries in polycrystalline materials; however, that technique requires substantially more measurement time than FF-HEDM and is, therefore, currently viewed as infeasible for mapping a complete volume of open-cell metal foam.

Despite the aforementioned limitations, the method and results presented here have important implications for a number of applications. First, we anticipate that the proposed framework could be used in applications involving ultra-low-density materials other than open-cell foams. One possibility would be to apply the framework to additively manufactured (AM) lattice structures or metamaterials [60–64] to relate sub-strut microstructural characteristics (viz., precipitates and grain structure) to overall mechanical response. Due to the regular periodic nature of lattice structures, the authors anticipate that the SCII ligament-tracking software would provide more complete tracking results when compared with the stochastic arrangement of ligaments in this work. This, in turn, would allow for more accurate grain tracking through deformation.

This work also has important implications on numerical modeling efforts for open-cell metal foams and lattice structures. While there have been efforts to model the mechanical response of open-cell metal foams under various loading scenarios (e.g., [6,65,66]), such models are particularly difficult to validate. However, the data obtained and the maps generated in this study will help to inform and/or validate numerical models, moving beyond the continuum scale to consider the effects of sub-ligament microstructures, namely grains and precipitates. Shade et al. [67] recently highlighted the potential for HEDM data sets

to enable new pathways for calibrating and validating crystal plasticity models. Grain-scale in situ data obtainable through such methods can be compared with numerical modeling results; the framework presented herein will be particularly valuable as a way of generating and tracking grain-scale features to be compared with numerical models for ultra-low-density polycrystalline materials.

5. Conclusions

The three-dimensional (3D) grain and precipitate structure of an intact volume of ultra-low-density open-cell metal foam containing multiple complete unit cells was characterized in situ during mechanical loading at the 1-ID beamline of the Advanced Photon Source. A 5 mm-diameter sample of 6% relative-density aluminum foam was subjected to compressive loading while μCT and FF-HEDM measurements were collected at interrupted displacement intervals. To accomplish these measurements, two primary challenges needed to be addressed. First, because the cell dimensions of the foam were approximately the same size as the width of the X-ray beam, the majority of the foam volume remained outside the extents of the beam throughout the experiment. To address this challenge, a scanning and stitching measurement and analysis procedure was implemented. At each displacement step, scanning and stage translation (both horizontal and vertical) were performed in sequence such that the complete volume of foam was fully characterized using both μCT and FF-HEDM. A special stitching algorithm was established in the FF-HEDM reconstruction software package to allow combining the detector diffraction image data from multiple scans in a given horizontal layer into one single detector image data set while avoiding subpixel-size shifts. The second was a data-analysis challenge pertaining to large rigid-body transformations that individual ligaments undergo during mechanical loading. Even for grains that exhibit little to no crystallographic reorientation during applied loading, such rigid-body transformations of the ligaments can significantly impact the representation of crystal orientation of a given grain from one displacement step to the next. To address this challenge and enable automated tracking of individual grains from step-to-step, a ligament-tracking software was used to first track the location, orientation, and dimensions of each ligament throughout the experiment. After assigning each grain to its parent ligament, the grain's crystal orientation could then be represented in the local, time-dependent, ligament reference frame rather than the global reference frame. Subsequently, a crystal-misorientation threshold was applied among displacement steps to track individual grains throughout the foam volume.

To our knowledge, the 3D grain maps presented in this work are the first of such kind for volumes of open-cell metal foams containing multiple complete unit cells. Furthermore, maps of precipitate structures, along with observed deformation evolution, support future studies into the relationship between precipitate content and ligament failure mechanisms. The measurements presented here have important implications on future modeling efforts, and the methods can be applied to other ultra-low-density materials and structures, including additively manufactured metal lattices.

Declaration of Competing Interest

The authors declare that they have no known competing financial interests or personal relationships that could have appeared to influence the work reported in this paper.

Data availability

Data will be made available on request. The raw/processed data required to reproduce these findings cannot be shared at this time as the data also forms part of an ongoing study.

Acknowledgement

This material is based upon work supported by the National Science Foundation under Grant No. CMMI-1629660. This research used resources of the Advanced Photon Source, a U.S. Department of Energy (DOE) Office of Science user facility at Argonne National Laboratory and is based on research supported by the U.S. DOE Office of Science-Basic Energy Sciences, under Contract No. DE-AC02-06CH11357.

Appendix A. Supplementary data

Supplementary data to this article can be found online at https://doi.org/10.1016/j.matchar.2022.112477.

References

[1] A.G. Evans, J. Hutchinson, M. Ashby, Multifunctionality of cellular metal systems, Prog. Mater Sci. 43 (1998) 171–221.
[2] T. Nieh, K. Higashi, J. Wadsworth, Effect of cell morphology on the compressive properties of open-cell aluminum foams, Mater. Sci. Eng. A 283 (2000) 105–110.
[3] J. Zhou, C. Mercer, W. Soboyejo, An investigation of the microstructure and strength of open-cell 6101 aluminum foams, Metall. Mater. Trans. A 33 (2002) 1413–1427.
[4] P. Kenesei, C. Kádár, Z. Rajkovits, J. Lendvai, The influence of cell-size distribution on the plastic deformation in metal foams, Scripta Mater. 50 (2004) 295–300.
[5] L. Gong, S. Kyriakides, W.-Y. Jang, Compressive response of open-cell foams. part i: Morphology and elastic properties, Int. J. Solids Struct. 42 (2005) 1355–1379.
[6] W.-Y. Jang, S. Kyriakides, On the crushing of aluminum open-cell foams: Part i. experiments, Int. J. Solids Struct. 46 (2009) 617–634.
[7] I. Gibson, M.F. Ashby, The mechanics of three-dimensional cellular materials, Proc. R. Soc. Lond. A: Math. Phys. Sci. 382 (1982) 43–59.
[8] M.F. Ashby, R. Medalist, The mechanical properties of cellular solids, Metall. Trans. A 14 (1983) 1755–1769.
[9] L.J. Gibson, M.F. Ashby, Cellular solids: structure and properties, Cambridge University Press, 1999.
[10] J. Zhou, Z. Gao, A. Cuitino, W. Soboyejo, Effects of heat treatment on the compressive deformation behavior of open cell aluminum foams, Mater. Sci. Eng. A 386 (2004) 118–128.
[11] P. Schüler, S.F. Fischer, A. Bührig-Polaczek, C. Fleck, Deformation and failure behaviour of open cell al foams under quasistatic and impact loading, Mater. Sci. Eng. A 587 (2013) 250–261.
[12] E. Amsterdam, P. Onck, J.T.M. De Hosson, Fracture and microstructure of open cell aluminum foam, J. Mater. Sci. 40 (2005) 5813–5819.
[13] P. Schüler, R. Frank, D. Uebel, S.F. Fischer, A. Bührig-Polaczek, C. Fleck, Influence of heat treatments on the microstructure and mechanical behaviour of open cell alsi7mg0. 3 foams on different lengthscales, Acta Mater. 109 (2016) 32–45.
[14] C. Petit, E. Maire, S. Meille, J. Adrien, Two-scale study of the fracture of an aluminum foam by x-ray tomography and finite element modeling, Mater. Des. 120 (2017) 117–127.
[15] J. Zhou, S. Allameh, W. Soboyejo, Microscale testing of the strut in open cell aluminum foams, J. Mater. Sci. 40 (2005) 429–439.
[16] V. Goussery, Y. Bienvenu, S. Forest, A.-F. Gourgues, C. Colin, J.-D. Bartout, Grain size effects on the mechanical behavior of open-cell nickel foams, Adv. Eng. Mater. 6 (2004) 432–439.
[17] Y. Wang, H. Huang, G. Jia, G. Ke, J. Zhang, G. Yuan, Effect of grain size on the mechanical properties of mg foams, J. Mater. Sci. Technol. 58 (2020) 46–54.
[18] J.C. Plumb, J.F. Lind, J.C. Tucker, R. Kelley, A.D. Spear, Three-dimensional grain mapping of open-cell metallic foam by integrating synthetic data with experimental data from high-energy x-ray diffraction microscopy, Mater. Charact. 144 (2018) 448–460.
[19] D.H. Bilderback, P. Elleaume, E. Weckert, Review of third and next generation synchrotron light sources, J. Phys. B: At. Mol. Opt. Phys. 38 (2005) S773.
[20] L. Wang, Z. Huang, H. Wang, A. Maldar, S. Yi, J.-S. Park, P. Kenesei, E. Lilleodden, X. Zeng, Study of slip activity in a mg-y alloy by in situ high energy x-ray diffraction microscopy and elastic viscoplastic self-consistent modeling, Acta Mater. 155 (2018) 138–152.
[21] A.D. Murphy-Leonard, D.C. Pagan, A. Beaudoin, M.P. Miller, J.E. Allison, Quantification of cyclic twinning-detwinning behavior during low-cycle fatigue of pure magnesium using high energy x-ray diffraction, Int. J. Fatigue 125 (2019) 314–323.
[22] D.C. Pagan, P.A. Shade, N.R. Barton, J.-S. Park, P. Kenesei, D.B. Menasche, J. V. Bernier, Modeling slip system strength evolution in ti-7al informed by in-situ grain stress measurements, Acta Mater. 128 (2017) 406–417.
[23] D. Naragani, M.D. Sangid, P.A. Shade, J.C. Schuren, H. Sharma, J.-S. Park, P. Kenesei, J.V. Bernier, T.J. Turner, I. Parr, Investigation of fatigue crack initiation from a non-metallic inclusion via high energy x-ray diffraction microscopy, Acta Mater. 137 (2017) 71–84.
[24] A.D. Spear, S.F. Li, J.F. Lind, R.M. Suter, A.R. Ingraffea, Three-dimensional characterization of microstructurally small fatigue-crack evolution using quantitative fractography combined with post-mortem x-ray tomography and high-energy x-ray diffraction microscopy, Acta Mater. 76 (2014) 413–424.

[25] R. Suter, D. Hennessy, C. Xiao, U. Lienert, Forward modeling method for microstructure reconstruction using x-ray diffraction microscopy: Single-crystal verification, Rev. Sci. Instrum. 77 (2006), 123905.
[26] U. Lienert, S. Li, C. Hefferan, J. Lind, R. Suter, J. Bernier, N. Barton, M. Brandes, M. Mills, M. Miller, et al., High-energy diffraction microscopy at the advanced photon source, Jom 63 (2011) 70–77.
[27] J.V. Bernier, N.R. Barton, U. Lienert, M.P. Miller, Far-field high-energy diffraction microscopy: a tool for intergranular orientation and strain analysis, J. Strain Anal. Eng. Des. 46 (2011) 527–547.
[28] J.-S. Park, X. Zhang, P. Kenesei, S.L. Wong, M. Li, J. Almer, Far-field high-energy diffraction microscopy: a non-destructive tool for characterizing the microstructure and micromechanical state of polycrystalline materials, Microsc. Today 25 (2017) 36–45.
[29] R. Pokharel, Overview of high-energy x-ray diffraction microscopy (hedm) for mesoscale material characterization in three-dimensions, in: Materials Discovery and Design, Springer, 2018, pp. 167–201.
[30] J.V. Bernier, R.M. Suter, A.D. Rollett, J.D. Almer, High-energy x-ray diffraction microscopy in materials science, Annu. Rev. Mater. Res. 50 (2020).
[31] R. Pokharel, J. Lind, S.F. Li, P. Kenesei, R.A. Lebensohn, R.M. Suter, A.D. Rollett, In-situ observation of bulk 3d grain evolution during plastic deformation in polycrystalline cu, Int. J. Plast 67 (2015) 217–234.
[32] L. Wang, Z. Zheng, H. Phukan, P. Kenesei, J.-S. Park, J. Lind, R. Suter, T.R. Bieler, Direct measurement of critical resolved shear stress of prismatic and basal slip in polycrystalline ti using high energy x-ray diffraction microscopy, Acta Mater. 132 (2017) 598–610.
[33] R. Pokharel, R.A. Lebensohn, D.C. Pagan, T.L. Ickes, B. Clausen, D.W. Brown, C.-F. Chen, D.S. Dale, J.V. Bernier, In-situ grain resolved stress characterization during damage initiation in cu-10% w alloy, Jom 72 (2020) 48–56.
[34] D.B. Menasche, W.D. Musinski, M. Obstalecki, M.N. Shah, S.P. Donegan, J. V. Bernier, P. Kenesei, J.-S. Park, P.A. Shade, Afrl additive manufacturing modeling series: challenge 4, in situ mechanical test of an in625 sample with concurrent high-energy diffraction microscopy characterization, Integr. Mater. Manuf. Innov. 10 (2021) 338–347.
[35] J.C. Schuren, P.A. Shade, J.V. Bernier, S.F. Li, B. Blank, J. Lind, P. Kenesei, U. Lienert, R.M. Suter, T.J. Turner, et al., New opportunities for quantitative tracking of polycrystal responses in three dimensions, Curr. Opin. Solid State Mater. Sci. 19 (2015) 235–244.
[36] M.P. Miller, D.C. Pagan, A.J. Beaudoin, K.E. Nygren, D.J. Shadle, Understanding micromechanical material behavior using synchrotron x-rays and in situ loading, Metall. Mater. Trans. A 51 (2020) 4360–4376.
[37] J. Banhart, Manufacture, characterisation and application of cellular metals and metal foams, Prog. Mater Sci. 46 (2001) 559–632.
[38] K.E. Matheson, K.K. Cross, M.M. Nowell, A.D. Spear, A multiscale comparison of stochastic open-cell aluminum foam produced via conventional and additive-manufacturing routes, Mater. Sci. Eng. A 707 (2017) 181–192.
[39] J.-S. Park, H. Sharma, P. Kenesei, Repeatability and sensitivity characterization of the far-field high-energy diffraction microscopy instrument at the advanced photon source, J. Synchrotron Radiat. 28 (2021).
[40] A. Khounsary, P. Kenesei, J. Collins, G. Navrotski, J. Nudell, High energy x-ray micro-tomography for the characterization of thermally fatigued glidcop specimen, in: Journal of Physics: Conference Series, vol. 425, IOP Publishing, 2013, p. 212015.
[41] J. Lee, J. Almer, C. Aydıner, J. Bernier, K. Chapman, P. Chupas, D. Haeffner, K. Kump, P. Lee, U. Lienert, et al., Characterization and application of a ge amorphous silicon flat panel detector in a synchrotron light source, Nucl. Instrum. Methods Phys. Res., Sect. A 582 (2007) 182–184.
[42] D. Kaiser, R. Watters, J.: National institute of standards & technology standard reference material674b x-ray powder diffraction intensity set for quantitative analysis by x-ray powder diffraction, Tech. rep., National Institute of Standards and Technology, 2007.
[43] A. Borbely, L. Renversade, P. Kenesei, J. Wright, On the calibration of high-energy x-ray diffraction setups. i. assessing tilt and spatial distortion of the area detector, J. Appl. Crystallogr. 47 (2014) 1042–1053.
[44] A. Borbély, L. Renversade, P. Kenesei, On the calibration of high-energy x-ray diffraction setups. ii. assessing the rotation axis and residual strains, J. Appl. Crystallogr. 47 (2014) 1585–1595.
[45] B.A. Dowd, G.H. Campbell, R.B. Marr, V.V. Nagarkar, S.V. Tipnis, L. Axe, D. P. Siddons, Developments in synchrotron x-ray computed microtomography at the national synchrotron light source, in: Developments in X-ray Tomography II, vol. 3772, International Society for Optics and Photonics, 1999, pp. 224–236.
[46] O. Ronneberger, P. Fischer, T. Brox, U-net: Convolutional networks for biomedical image segmentation, in: International Conference on Medical image computing and computer-assisted intervention, Springer, 2015, pp. 234–241.
[47] C.A. Schneider, W.S. Rasband, K.W. Eliceiri, Nih image to imagej: 25 years of image analysis, Nat. Methods 9 (2012) 671–675.
[48] H. Sharma, R.M. Huizenga, S.E. Offerman, A fast methodology to determine the characteristics of thousands of grains using three-dimensional x-ray diffraction. i. overlapping diffraction peaks and parameters of the experimental setup, J. Appl. Crystallogr. 45 (2012) 693–704.
[49] H. Sharma, R.M. Huizenga, S.E. Offerman, A fast methodology to determine the characteristics of thousands of grains using three-dimensional x-ray diffraction. ii. volume, centre-of-mass position, crystallographic orientation and strain state of grains, J. Appl. Crystallogr. 45 (2012) 705–718.
[50] M.A. Groeber, M.A. Jackson, Dream. 3d: a digital representation environment for the analysis of microstructure in 3d, Integr. Mater. Manuf. Innov. 3 (2014) 5.
[51] J.C. Tucker, A.D. Spear, A tool to generate grain-resolved open-cell metal foam models, Integr. Mater. Manuf. Innov. 8 (2019) 247–256.
[52] J. Ahrens, B. Geveci, C. Law, Paraview: An end-user tool for large data visualization, Visualization Handbook 717 (2005).
[53] S. Petruzza, A. Gyulassy, S. Leventhal, J.J. Baglino, M. Czabaj, A.D. Spear, V. Pascucci, High-throughput feature extraction for measuring attributes of deforming open-cell foams, IEEE Trans. Visual Comput. Graphics 26 (2019) 140–150.
[54] R. Brannon, Rotation, reflection, and frame changes, IOP Publishing, 2018.
[55] A. Jung, J. Luksch, S. Diebels, F. Schäfer, C. Motz, In-situ and ex-situ microtensile testing of individual struts of al foams and ni/al hybrid foams, Mater. Des. 153 (2018) 104–119.
[56] P. Chen, S. Mao, Y. Liu, F. Wang, Y. Zhang, Z. Zhang, X. Han, In-situ ebsd study of the active slip systems and lattice rotation behavior of surface grains in aluminum alloy during tensile deformation, Mater. Sci. Eng. A 580 (2013) 114–124.
[57] M. Winning, G. Gottstein, L. Shvindlerman, Migration of grain boundaries under the influence of an external shear stress, Mater. Sci. Eng. A 317 (2001) 17–20.
[58] W. Hosford Jr, Plane-strain compression of aluminum crystals, Acta Metall. 14 (1966) 1085–1094.
[59] S. Li, R. Suter, Adaptive reconstruction method for three-dimensional orientation imaging, J. Appl. Crystallogr. 46 (2013) 512–524.
[60] M. Leary, M. Mazur, J. Elambasseril, M. McMillan, T. Chirent, Y. Sun, M. Qian, M. Easton, M. Brandt, Selective laser melting (slm) of alsi12mg lattice structures, Mater. Des. 98 (2016) 344–357.
[61] M. Mazur, M. Leary, S. Sun, M. Vcelka, D. Shidid, M. Brandt, Deformation and failure behaviour of ti-6al-4v lattice structures manufactured by selective laser melting (slm), Int. J. Adv. Manuf. Technol. 84 (2016) 1391–1411.
[62] R. Wauthle, B. Vrancken, B. Beynaerts, K. Jorissen, J. Schrooten, J.-P. Kruth, J. Van Humbeeck, Effects of build orientation and heat treatment on the microstructure and mechanical properties of selective laser melted ti6al4v lattice structures, Addit. Manuf. 5 (2015) 77–84.
[63] M. Leary, M. Mazur, H. Williams, E. Yang, A. Alghamdi, B. Lozanovski, X. Zhang, D. Shidid, L. Farahbod-Sternahl, G. Witt, et al., Inconel 625 lattice structures manufactured by selective laser melting (slm): mechanical properties, deformation and failure modes, Mater. Des. 157 (2018) 179–199.
[64] C. Yan, L. Hao, A. Hussein, P. Young, J. Huang, W. Zhu, Microstructure and mechanical properties of aluminium alloy cellular lattice structures manufactured by direct metal laser sintering, Mater. Sci. Eng. A 628 (2015) 238–246.
[65] W.-Y. Jang, A.M. Kraynik, S. Kyriakides, On the microstructure of open-cell foams and its effect on elastic properties, Int. J. Solids Struct. 45 (2008) 1845–1875.
[66] D. Zhao, K.E. Matheson, B.R. Phung, S. Petruzza, M.W. Czabaj, A.D. Spear, Investigating the effect of grain structure on compressive response of open-cell metal foam using high-fidelity crystal-plasticity modeling, Mater. Sci. Eng. A 812 (2021), 140847.
[67] P.A. Shade, W.D. Musinski, M. Obstalecki, D.C. Pagan, A.J. Beaudoin, J.V. Bernier, T.J. Turner, Exploring new links between crystal plasticity models and high-energy x-ray diffraction microscopy, Curr. Opin. Solid State Mater. Sci. 23 (2019), 100763.